

Weak Gravitational Lensing by Dark Clusters

Nevin N. Weinberg and Marc Kamionkowski

California Institute of Technology, Mail Code 130-33, Pasadena, CA 91125 USA

March 2002

ABSTRACT

We calculate the abundance of dark-matter concentrations that are sufficiently over-dense to produce a detectable weak-gravitational-lensing signal. Most of these over-densities are virialized halos containing identifiable X-ray and/or optical clusters. However, a significant fraction are nonvirialized overdensities still in the process of gravitational collapse—these should produce significantly weaker or no X-ray emission. Our predicted abundance of such dark clusters are consistent with the abundance implied by the Erben et al. (2000) detection of a dark lens. Weak lensing by these nonvirialized objects will need to be considered when determining cosmological parameters with the lens abundance in future weak-lensing surveys. Such weak lenses should also help shed light on the process of cluster formation.

Key words: galaxy clusters—weak gravitational lensing—cosmology

1 INTRODUCTION

Weak gravitational lensing due to the deep gravitational potential of a galaxy cluster gives rise to a detectable weak distortion of the images of background galaxies. This weak shear has now been detected around roughly 30 clusters and been used to map the total dark-matter mass in the clusters as well as the dark-matter distributions within the clusters (see Bartelmann & Schneider 2001, Mellier 1999). Weak lensing also has the potential to map the mass distribution on even larger scales (Miralda-Escudé 1991; Blandford et al. 1991; Kaiser 1992; Bartelmann & Schneider 1992; Stebbins 1997; Kamionkowski et al. 1998). Just last year, four groups independently reported detection of cosmic shear, distortions to background galaxies induced by weak gravitational lensing by mass inhomogeneities on *few*-Mpc scales along the line of sight (Bacon et al. 2000; Kaiser et al. 2000; Wittman et al. 2000; Van Waerbeke et al. 2000). It is apparent that in the future, such cosmic-shear surveys will have the sensitivity to identify galaxy clusters in the field. Since such surveys will probe the *total* mass directly, it could provide a powerful new technique for determining the cluster-halo abundance and thus the power-spectrum amplitude σ_8 and matter density Ω_m (e.g., Kruse & Schneider 1999; Reblinsky et al. 1999).

In fact, one spectroscopically-confirmed cluster has already been detected via its gravitational-lensing effect on background galaxies (Wittman et al. 2001). More intriguing is the apparent dark lens discovered by Erben et al. (2000). This lensing signal corresponds to a $\sim 10^{14} M_\odot$ mass concentration, but there is no obvious corresponding galaxy overdensity (Gray et al. 2001) and only faint (if any) X-ray emission. Evidence for other apparent dark lenses has been reported by Miralles et al. (2002) and Koopmans et al. (2000), the latter involving a detection through strong, rather than weak, lensing.

In retrospect, the existence of such dark concentrations should not come as too much of a surprise. Galaxy clusters form at rare (e.g., $> 3\sigma$) high-density peaks of a Gaussian primordial distribution. Thus, for every virialized cluster, there should be a significant number of proto-clusters (e.g., $2\sigma - 3\sigma$ peaks), mass overdensities that have not yet undergone gravitational collapse and virialized, but which have begun to break away from the cosmological expansion. The timescale for collapse of cluster-mass objects is large, and the overdensities can be very large even before they have virialized. It should thus not be too surprising if such objects produce a weak-lensing signal that resembles that from virialized clusters.

These proto-clusters should contain galaxies and maybe a few groups that later merge to form the cluster. Since the X-ray luminosity is a very rapidly varying function of the virialized mass, the summed X-ray emission from these objects should be much smaller than that from a fully virialized cluster of the same mass. When we refer to these proto-clusters as “dark,” we thus mean that they should be X-ray underluminous. Strictly speaking, the mass-to-light ratios of these clusters should be comparable to those for ordinary clusters. However, high-redshift clusters may be difficult to pick out in galaxy surveys, and these proto-clusters should have a sky density a few times smaller. Thus it would not be surprising if these dark lenses had no readily apparent corresponding galaxy overdensity.

In this paper we calculate the abundance of dark and virialized lenses. To do so, we first determine the overdensity required to produce a detectable weak-lensing signal as a function of redshift. We consider several different density profiles including a homogeneous sphere, an isothermal sphere, a Navarro, Frenk, & White (Navarro et al. 1997; Navarro et al. 1996; Navarro

et al. 1995) profile and a Hernquist (Hernquist 1990) profile. We then use the spherical-top-hat-collapse (STHC) model to determine the differential abundance of overdensities as a function of position along their evolutionary cycle. This allows us to determine the sky density and redshift distribution of halos that are sufficiently overdense to produce a weak-lensing signal. As our results below will show, there should be roughly one dark lens for every 5–10 virialized lenses discovered by weak lensing. Furthermore, given the sky coverage and average image size of weak-lensing maps to date, the number of dark lenses we would expect to have seen is of order unity and therefore consistent with the detection (Erben et al. (2000), Miralles et al. 2002) of one or two dark lenses.

2 MINIMUM OVERDENSITY REQUIRED TO PRODUCE WEAK-LENSING SIGNAL

In this Section we provide the conditions for an overdensity of mass M and radius R at redshift z to produce a detectable weak-lensing signal. Following the procedure of Bartelmann & Schneider (2001) (see also Schneider 1996, Seitz & Schneider 1997, Kruse & Schneider 1999) we determine the dependence of a lensing system's signal-to-noise ratio on that system's overdensity and redshift.

In a weak-lensing map, a mass overdensity causes the image of the background source galaxies to be tangentially sheared. Noise is introduced by both the intrinsic ellipticity of these background galaxies as well as by the presence of foreground galaxies in the image. To arrive at a signal-to-noise relation for a weak-lensing system, consider N galaxy images each at angular position $\boldsymbol{\theta}_i = (\theta_i \cos \phi_i, \theta_i \sin \phi_i)$ with tangential ellipticity $\epsilon_t(\boldsymbol{\theta}_i)$ and within a lens-centered annulus that is bounded by angular radii $\theta_{\text{in}} \leq \theta_i \leq \theta_{\text{out}}$. The shear γ is related linearly to the dimensionless surface mass density of the lens, which is the physical surface mass density $\Sigma(\boldsymbol{\theta})$ divided by the critical surface mass density Σ_{crit} . For a lens at redshift z_d and a source at redshift z_s ,

$$\Sigma_{\text{crit}}(z_d; z_s) = \frac{c^2}{4\pi G} \frac{D_s}{D_d D_{ds}}, \quad (1)$$

where D_d , D_s and D_{ds} are the angular-diameter distances between the lens and the observer, the source galaxy and the observer, and the lens and the source, respectively. To account for the redshift distribution of the source galaxies, define (Seitz & Schneider 1997)

$$Z(z_s; z_d) \equiv \frac{\lim_{z_s \rightarrow \infty} \Sigma_{\text{crit}}(z_d; z_s)}{\Sigma_{\text{crit}}(z_d; z_s)} = \frac{\Sigma_{\text{crit}\infty}(z_d)}{\Sigma_{\text{crit}}(z_d; z_s)}. \quad (2)$$

Then the dimensionless surface mass density is given by,

$$\kappa(\boldsymbol{\theta}, z_s) = \frac{\Sigma(\boldsymbol{\theta})}{\Sigma_{\text{crit}}} = \frac{\Sigma(\boldsymbol{\theta})}{\Sigma_{\text{crit}\infty}} \frac{\Sigma_{\text{crit}\infty}}{\Sigma_{\text{crit}}} \equiv \kappa(\boldsymbol{\theta}) Z(z_s; z_d). \quad (3)$$

Furthermore, the linear relation between the shear and surface mass density implies that they have the same dependence on source redshift so that $\gamma(\boldsymbol{\theta}, z_s) \equiv Z(z_s; z_d)\gamma(\boldsymbol{\theta})$. For the rest of this paper any reference to κ or γ refers to $\kappa(\boldsymbol{\theta})$ and $\gamma(\boldsymbol{\theta})$, respectively. Assuming the intrinsic orientation of galaxy sources is random, the expectation value of the image ellipticity is (Seitz & Schneider 1997; Bartelmann & Schneider 2001)

$$E(\epsilon) \approx \langle Z \rangle \gamma(\boldsymbol{\theta}), \quad (4)$$

where

$$\langle Z \rangle = \int dz_s p_z(z_s) Z(z_s; z_d), \quad (5)$$

and $p_z(z_s)$ is the redshift distribution of source galaxies. The function $\langle Z \rangle = \langle Z \rangle(z_d)$ —of order unity for the redshifts considered—allows a source redshift distribution to be collapsed onto a single redshift z_s satisfying $Z(z_s) = \langle Z \rangle$ (see Bartelmann & Schneider 2001).

Using the M_{ap} -statistics introduced by Schneider (1996), define a discretized estimator for the spatially filtered mass inside a circular aperture of angular radius θ ,

$$M_{\text{ap}} \equiv \frac{1}{n} \sum_{i=1}^N \epsilon_t(\boldsymbol{\theta}_i) Q(|\boldsymbol{\theta}_i|), \quad (6)$$

where n is the number density of galaxy images and Q is a weight function that will be chosen later so as to maximize the signal-to-noise ratio of the estimator. Assuming the ellipticities of different images are uncorrelated the dispersion of M_{ap} can be obtained by squaring (6) and taking the expectation value, yielding

$$\sigma^2 = \frac{\sigma_\epsilon^2}{2n^2} \sum_{i=1}^N Q^2(|\boldsymbol{\theta}_i|), \quad (7)$$

where σ_ϵ is the dispersion of the two component ellipticity. By (4) the expectation value of M_{ap} is,

$$\langle M_{\text{ap}} \rangle = \frac{\langle Z \rangle}{n} \sum_{i=1}^N \gamma_t(\theta_i) Q(|\theta_i|), \quad (8)$$

where γ_t is the tangential shear. Taking the ensemble average of (8) over the probability distribution for the galaxy positions gives,

$$\langle M_{\text{ap}} \rangle_c = 2\pi \langle Z \rangle \int_{\theta_{\text{in}}}^{\theta_{\text{out}}} d\theta \theta \langle \gamma_t \rangle(\theta) Q(\theta), \quad (9)$$

where $\langle \gamma_t \rangle(\theta)$ is the mean tangential shear on a circle of angular radius θ and the subscript ‘c’ stands for continuous. Similarly, we can take the ensemble average of the dispersion (7), to obtain

$$\sigma_c^2 = \frac{\pi \sigma_\epsilon^2}{n} \int_{\theta_{\text{in}}}^{\theta_{\text{out}}} d\theta \theta Q^2(\theta). \quad (10)$$

The ensemble-averaged signal-to-noise ratio is then,

$$\frac{S}{N} = \frac{\langle M_{\text{ap}} \rangle_c}{\sigma_c} = \frac{2\langle Z \rangle \sqrt{\pi n}}{\sigma_\epsilon} \frac{\int_{\theta_{\text{in}}}^{\theta_{\text{out}}} d\theta \theta \langle \gamma_t \rangle(\theta) Q(\theta)}{\sqrt{\int_{\theta_{\text{in}}}^{\theta_{\text{out}}} d\theta \theta Q^2(\theta)}}. \quad (11)$$

By the Cauchy-Schwarz inequality the signal-to-noise ratio of the estimator is maximized if

$$Q(\theta) \propto \langle \gamma_t \rangle(\theta). \quad (12)$$

Since

$$\langle \gamma_t \rangle(\theta) = \bar{\kappa}(\theta) - \langle \kappa \rangle(\theta), \quad (13)$$

(Bartelmann 1995) where $\langle \kappa \rangle(\theta)$ is the dimensionless mean surface mass density on a circle of radius θ and $\bar{\kappa}(\theta)$ is the dimensionless mean surface mass density within a circle of radius θ , the maximized signal-to-noise ratio becomes

$$\frac{S}{N} = \frac{2\langle Z \rangle \sqrt{\pi n}}{\sigma_\epsilon} \sqrt{\int_{\theta_{\text{in}}}^{\theta_{\text{out}}} d\theta \theta [\bar{\kappa}(\theta) - \langle \kappa \rangle(\theta)]^2}. \quad (14)$$

To compute the signal-to-noise ratio for a lens with a given density profile we need to determine the mean tangential shear of the source galaxies. Different density profiles will in general produce different shear patterns. In particular, the more cuspy a profile is the stronger its lensing signal. Of course this becomes more complicated when considering profiles with power-law breaks. For instance, although the NFW profile goes as r^{-1} at small radii while the isothermal sphere goes as r^{-2} , at larger radii the former varies as r^{-3} while the latter remains at r^{-2} . The net effect, as we will show, is that the NFW profile yields a stronger signal compared to the isothermal sphere for lenses at reasonable redshifts. That said, we consider a variety of profiles to account for the full range of possibilities and to study the dependence of our results on these profiles. Specifically, we compare the calculated abundances assuming the overdensity is a point mass, a uniform-density sphere, an isothermal sphere, an NFW profile and a Hernquist profile. Note that for an overdensity with angular radius smaller than the size of the lensing image, the shear pattern at the outer radius will be that of a point mass. Furthermore, if the angular radius is larger than the image size then the lensing signal is determined by just the mass M_P within the projected image radius $P = \theta_{\text{out}} D_d$ and not the mass outside this radius. The derivation of the signal-to-noise relation for each of these profiles is given in the Appendix.

To produce a detectable signal, an overdensity must be large enough to yield a signal-to-noise ratio greater than some minimum value. For the calculations done in this paper we adopt the following fiducial values, unless stated otherwise: $(S/N)_{\text{min}} = 5$, $\theta_{\text{out}} = 5$ arcmin, the number density of galaxy images is $n = 30$ arcmin $^{-2}$, and $\sigma_\epsilon = 0.2$. The minimum nonlinear overdensity corresponds to a particular position along the linear-theory evolutionary cycle. In the next Section we discuss how we relate the minimum *nonlinear* overdensity to a corresponding minimum *linear*-theory overdensity. This will enable us to apply the Press-Schechter formalism to obtain an estimate of the abundance of overdensities that produce a weak-lensing signal as a function of redshift.

3 DYNAMICS

We use the STHC model to relate the minimum non-linear overdensity needed for a detectable weak-lensing signal at a given redshift to a minimum linear-theory overdensity. According to STHC the non-linear evolution of cosmic density fluctuations is approximated by a dynamical model in which the initial linear perturbation is an isolated, uniform sphere surrounded by unperturbed matter. Gravitational instability causes the initially small linear perturbation to grow and enter the nonlinear regime, ultimately forming a virialized object that is decoupled from the cosmological background. In order to avoid the collapse to infinite density predicted by the solution of STHC, we invoke a simple smoothing scheme that allows us to map a linear overdensity greater than the critical linear density contrast, $\delta_c \sim 1.69$, to a finite nonlinear overdensity. In what follows

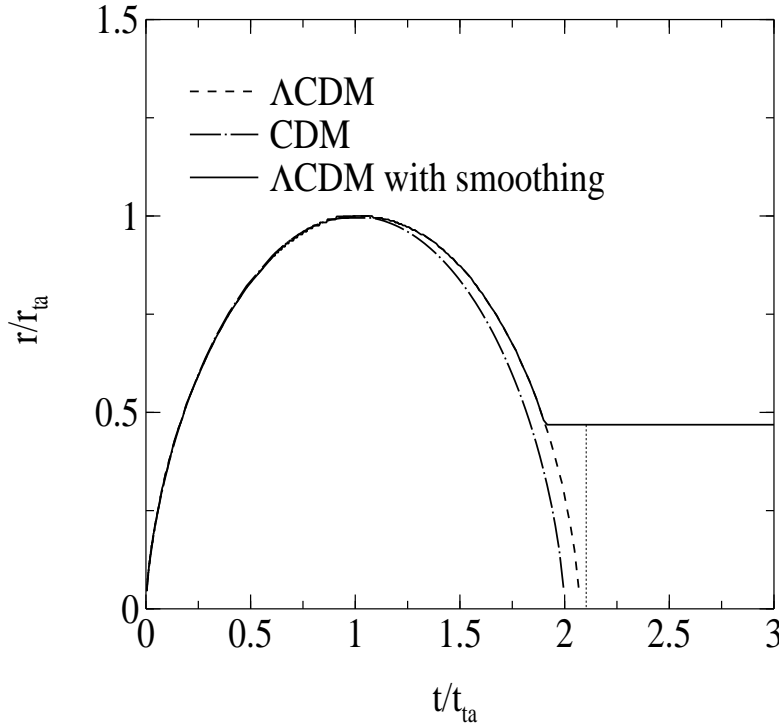


Figure 1. The radial evolution of a density perturbation according to the STHC model. At the turnaround time, $t = t_{ta}$, the perturbation reaches a maximum-expansion radius and begins to collapse. As expected, in a Λ CDM cosmology (dashed curve) the collapse takes somewhat longer than in a CDM cosmology (line-dot curve). The collapse to a singularity predicted by the solution of the STHC model is avoided by the smoothing scheme (solid curve) which yields a constant radius once the virialized overdensity is reached.

we shall consider the STHC model in a Λ CDM universe. Following the derivation of the relevant STHC formula, we present our smoothing scheme. Finally, we discuss how we distinguish ‘‘virialized’’ clusters from those that have not yet collapsed.

For a flat cosmology with a cosmological constant, the change in the proper radius, r , with scale factor a for a uniform spherical overdensity of fixed mass M is given by (see Peebles 1984, Eke et al. 1996)

$$\left(\frac{dr}{da}\right)^2 = \frac{r^{-1} + \omega r^2 - \beta}{a^{-1} + \omega a^2}, \quad (15)$$

where $a = (1 + z)^{-1}$, β is a constant which is positive for overdensities and

$$\omega = (\Omega_0^{-1} - 1), \quad (16)$$

where Ω_0 is the cosmological density parameter. Note that the units of r are such that $(3M/4\pi\rho_0)^{1/3} \equiv 1$ where ρ_0 is the cosmological background density at $z = 0$. Separating the variables in equation (15) and integrating gives

$$\int_0^r \frac{r'^{1/2}}{(\omega r'^3 - \beta r' + 1)^{1/2}} dr' = \int_0^a \frac{a'^{1/2}}{(\omega a'^3 + 1)^{1/2}} da'. \quad (17)$$

Solving for the root of the numerator in equation (15) gives the turnaround radius (i.e., radius at maximum expansion), r_{ta} , as a function of the density parameter ω and perturbation amplitude β . An exact solution for r_{ta} is given in Appendix A of Eke et al. (1996). For overdensities that are past turnaround the left-hand side of equation (17) is integrated from zero to r_{ta} and added to the integral from r to r_{ta} . The evolution of the radius of an overdensity as a function of time is illustrated in Figure 1. Note that the cosmological constant has the effect of slowing the collapse as compared to a CDM universe.

The non-linear overdensity is given by

$$1 + \delta^{NL} = \frac{\rho_{\text{pert}}}{\rho_b}, \quad (18)$$

where ρ_{pert} is the mean density of the perturbed region and ρ_b is the background density at the given redshift. Since $\rho_{\text{pert}} = \rho_0/r^3$ and $\rho_b = \rho_0/a^3$, the non-linear overdensity becomes

$$1 + \delta^{NL} = \left(\frac{a}{r}\right)^3. \quad (19)$$

For a given non-linear overdensity of mass M at redshift z we can find the radius of the perturbation r and can therefore solve equation (17) for β .

We now relate this same β to the linear-theory perturbation amplitude. Eke et al.(1996) showed that

$$\beta = \frac{a_0(2\omega)^{1/3}}{3A(a_0(2\omega)^{1/3})} \delta_0^{\text{lin}}, \quad (20)$$

where a_0 is the scale factor today, δ_0^{lin} is the linear-theory overdensity extrapolated to the present and

$$A(x) = \frac{(x^3 + 2)^{1/2}}{x^{3/2}} \int^x \left(\frac{u}{u^3 + 2}\right)^{3/2} du, \quad (21)$$

(Peebles 1980). The linear-theory overdensity at redshift z is given by

$$\delta^{\text{lin}}(z) = \delta_0^{\text{lin}} D(a), \quad (22)$$

where $D(a)$, the linear theory growth factor for a Λ CDM cosmology, is

$$D(a) = \frac{A(a(2\omega)^{1/3})}{A(a_0(2\omega)^{1/3})}. \quad (23)$$

Using equations (20), (22), and (23) we get the desired relation between the linear-theory overdensity and β :

$$\delta^{\text{lin}}(z) = 3\beta \frac{A(a(2\omega)^{1/3})}{a_0(2\omega)^{1/3}}. \quad (24)$$

Equations (17), (19) and (24) therefore provide a map between the non-linear overdensity and the linear-theory overdensity at a given redshift.

It can be shown that $r \rightarrow 0$ in the limit that $\delta^{\text{lin}} \rightarrow \delta_c$, corresponding to the well known infinite density predicted by the solution of STHC. An actual overdensity will, of course, virialize before reaching the singular solution. To properly account for this we introduce the following smoothing scheme.

Rather than assuming that an overdensity satisfies equation (19) throughout its evolution, assume it satisfies it only until it reaches the virialized overdensity $1 + \delta_{\text{vir}}^{\text{NL}}(z)$. Once the perturbation reaches the virialized overdensity take its radius to be a constant with time so that the overdensity continues to grow only because the cosmological background density keeps decreasing. The non-linear overdensity is therefore given by

$$1 + \delta^{\text{NL}} = \begin{cases} \left(\frac{a(t)}{r}\right)^3, & \text{if } \left(\frac{a(t)}{r}\right)^3 \leq 1 + \delta_{\text{vir}}^{\text{NL}}(z); \\ (1 + \delta_{\text{vir}}^{\text{NL}}) \left(\frac{a(t)}{a_{\text{vir}}}\right)^3, & \text{otherwise,} \end{cases} \quad (25)$$

where a_{vir} is the scale factor at virialization. Since $\delta^{\text{lin}}(t_2) = \delta^{\text{lin}}(t_1)D(a_2)/D(a_1)$, the linear-theory overdensity then becomes

$$\delta^{\text{lin}} = \begin{cases} 3\beta \frac{A(a(2\omega)^{1/3})}{A(a_0(2\omega)^{1/3})}, & \text{if } 1 + \delta^{\text{NL}} \leq 1 + \delta_{\text{vir}}^{\text{NL}}(z); \\ \delta^{\text{lin}}(a_{\text{vir}}) \frac{D(a(t))}{D(a_{\text{vir}})}, & \text{otherwise.} \end{cases} \quad (26)$$

Therefore, if the minimum non-linear overdensity needed to produce a detectable weak-lensing signal at redshift z is larger than the virialization overdensity, we evaluate a_{vir} using equation (25) and then compute the minimum linear-theory overdensity using the lower expression in equation (26). In Figure 1 we plot the radius of an overdensity as a function of time using this smoothing scheme. In Figure 2 we show the non-linear overdensity as a function of the linear-theory overdensity. Note that the value of the overdensity at virialization can be obtained by assuming $r = r_{\text{vir}}$, the virialized radius, in equation (19), and using the expression from Lahav et al. (1991) which gives the ratio between the turnaround radius and the virialization radius. For convenience we use the Kitayama & Suto (1996) approximation to $1 + \delta_{\text{vir}}^{\text{NL}}(z)$, as well as their approximation to $\delta_c(z)$. We independently verified that both approximations matched the solution of the exact formalism described above.

In summary, given the minimum non-linear overdensity needed to produce a detectable weak-lensing signal, $\delta_{\text{min}}^{\text{NL}}$, of an object of mass M at redshift z , we use equations (17), (25) and (26) to compute the corresponding minimum linear-theory overdensity, $\delta_{\text{min}}^{\text{lin}}$, needed to produce a detectable weak-lensing signal. If $\delta_{\text{min}}^{\text{lin}} < \delta_c(z)$ then the object can produce a detectable weak gravitational lens, even though it is not yet virialized.

4 ABUNDANCES

To calculate the abundance of overdensities that produce a weak-lensing signal as a function of redshift, we use Press-Schechter theory assuming Gaussian statistics for the initial linear-theory density field. The differential number count of lensing objects with mass larger than M per steradian, per unit redshift interval is

$$\frac{dN(> M, \delta_{\text{min}}^{\text{lin}})}{dz d\Omega} = \frac{dN(> M, \delta_{\text{min}}^{\text{lin}})}{dV} \frac{dV}{dz d\Omega}, \quad (27)$$

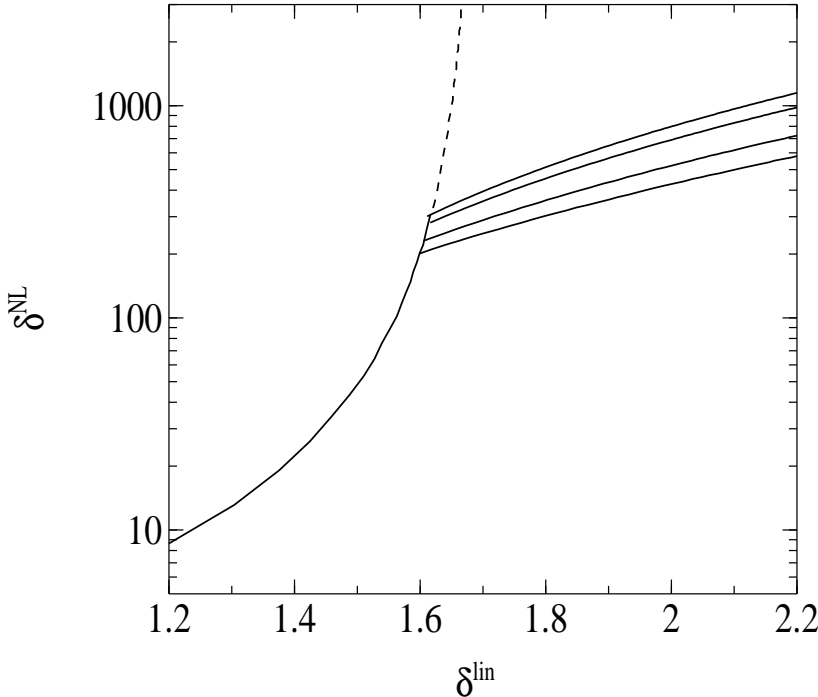


Figure 2. The nonlinear overdensity as a function of the linear-theory overdensity according to the STHC model. The full solution of the STHC model predicts collapse to an infinite overdensity as $\delta_{\text{lin}}^{\text{L}} \rightarrow 1.69$ (dashed curve). According to the smoothing scheme, however, once a mass concentration reaches the virialization overdensity $1 + \delta_{\text{vir}}^{\text{NL}}(z)$, its radius remains constant so that the overdensity increases in proportion to the decrease in the background density. The solid curves show the smoothing scheme solution for mass concentrations that reach the virialization overdensity at $z = 0.1, 0.2, 0.5$, and 1.0 , from top to bottom. In an Einstein-de Sitter Universe, the virialization overdensity is independent of redshift and therefore all of the solid curves would be the same.

where

$$\frac{dV}{dzd\Omega} = \frac{c}{H_0} \frac{(1+z)^2 D(z)^2}{\sqrt{\Omega_0(1+z)^3 + 1 - \Omega_0}}, \quad (28)$$

is the comoving-volume element, c is the speed of light, H_0 is Hubble's constant, and $D(z)$ is the angular-diameter distance at redshift z . The number density is given by

$$\frac{dN(> M, \delta_{\text{min}}^{\text{lin}})}{dV} = \int_M^\infty f(M; \delta_{\text{min}}^{\text{lin}}) \frac{dn}{dM}(M) dM, \quad (29)$$

where $dn(M)/dM$, the comoving number density of virialized objects of mass M in the interval dM , is (Press & Schechter 1974)

$$\frac{dn}{dM}(M) = \sqrt{\frac{2}{\pi}} \frac{\rho_0}{M^2} \frac{\delta_c(z)}{\sigma(M, z)} \left| \frac{d \ln \sigma}{d \ln M} \right| \exp \left[-\frac{\delta_c(z)^2}{2\sigma^2} \right]. \quad (30)$$

In this paper we use the Viana & Liddle (1999) fits to the dispersion of the density field, $\sigma(M, z)$, obtained from the galaxy cluster X-ray temperature distribution function. The function $f(M; \delta_{\text{min}}^{\text{lin}})$ is the fraction of objects, either dark or virialized, that can lens ($\delta > \delta_{\text{min}}^{\text{lin}}$) relative to those that are virialized ($\delta > \delta_c$). The probability that an object's linear overdensity is in the range $\delta_1 < \delta < \delta_2$ is

$$P(\delta_1 < \delta < \delta_2) = \text{erf} \left(\frac{\delta_2}{\sqrt{2}\sigma(M, z)} \right) - \text{erf} \left(\frac{\delta_1}{\sqrt{2}\sigma(M, z)} \right), \quad (31)$$

where 'erf' is the error function. Therefore, for dark lenses (i.e., those objects with $\delta_{\text{min}}^{\text{lin}} < \delta < \delta_c$)

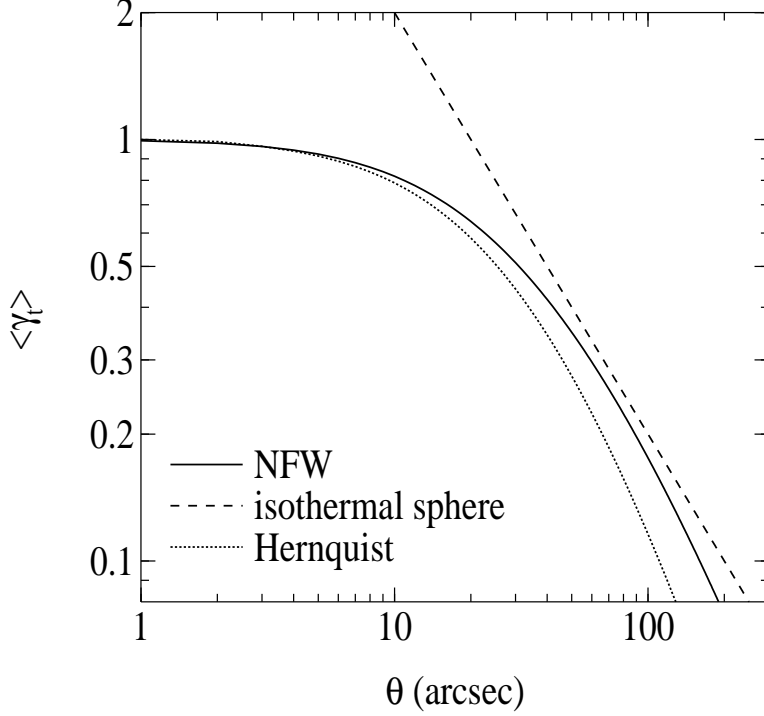


Figure 3. The mean tangential shear as a function of angular distance from the lens center for an NFW (solid curve), Hernquist (dotted curve) and isothermal sphere (dashed curve) density profile. The normalization is arbitrary.

$$f_{\text{dark}}(M; \delta_{\min}^{\text{lin}}) = \begin{cases} \frac{P(\delta_{\min}^{\text{lin}} < \delta < \delta_c)}{P(\delta > \delta_c)} & \delta_{\min}^{\text{lin}} < \delta_c; \\ 0, & \text{otherwise,} \end{cases} \quad (32)$$

while for virialized lenses ($\delta > \delta_c$ and $\delta > \delta_{\min}^{\text{lin}}$),

$$f_{\text{vir}}(M; \delta_{\min}^{\text{lin}}) = \begin{cases} \frac{P(\delta > \delta_{\min}^{\text{lin}})}{P(\delta > \delta_c)}, & \delta_{\min}^{\text{lin}} > \delta_c; \\ 1, & \text{otherwise.} \end{cases} \quad (33)$$

Integrating equation (27) over redshift assuming $f = f_{\text{dark}}$ yields the number count of dark lenses per unit area on the sky and similarly for virialized lenses when $f = f_{\text{vir}}$.

5 RESULTS

5.1 Minimum overdensity as a function of redshift

We can now compute the sky density of weak lenses. To gain physical insight into the results as well as illustrate the calculational procedure discussed above we first show the redshift dependence of the minimum non-linear overdensity. As noted earlier, the result is sensitive to the lens density profile on account of the minimum overdensity's dependence on the shear. Since the shear is proportional to the surface mass density, the NFW and Hernquist profiles (for whom $\rho \propto r^{-1}$ as $r \rightarrow 0$) have a constant shear at small radii while the isothermal sphere profile ($\rho \propto r^{-2}$) has a shear that goes as r^{-1} for all radii. This is shown in Figure 3, where we plot the radial dependence of the mean tangential shear for these different profiles.

In Figure 4, the minimum non-linear overdensity as a function of redshift for a $10^{14} M_{\odot}$ object is plotted for the various profiles. All the profiles show the same general trend: a minimum at $z \sim 0.3$ and monotonic rises at lower and higher redshifts. This is a consequence of the source-galaxy redshift distribution which we assume is given by a function of the form

$$p_z(z_s) = \frac{\beta z_s^2}{\Gamma(3/\beta) z_0^3} \exp \left[-(z_s/z_0)^{\beta} \right], \quad (34)$$

(e.g., Brainerd et al. 1996) with $\beta = 1.5$ and mean redshift $\langle z_s \rangle \approx 1.5z_0 = 1.2$. Since lenses are most effective when they lie

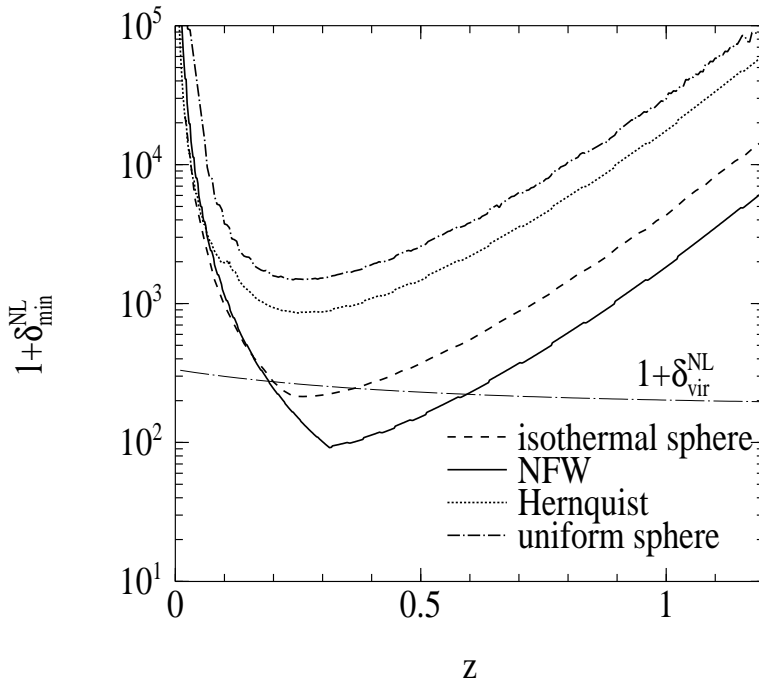


Figure 4. The minimum nonlinear overdensity needed to produce a detectable weak lensing signal as a function of redshift for a $10^{14} M_{\odot}$ object with a density profile that is a uniform-density sphere (line-dot curve), a truncated isothermal sphere (dashed curve), a Hernquist profile (dotted curve), and an NFW profile (solid curve). An overdensity with a larger mass will displace these curves downwards. The thin, long-dash-dot curve is the overdensity at virialization in the STHC model.

midway between the source and the observer (i.e., the factor $D_d D_{ds} / D_s$ peaks when $D_d \simeq D_{ds}$), an overdensity at $z \sim 0.3$ is ideally positioned to lens source galaxies that are primarily located at $z = \langle z_s \rangle \sim 1$, thereby accounting for the minimum in the curves. Accordingly, overdensities located at lower and higher redshifts than $z \sim 0.3$ are less effective at lensing so that a larger overdensity is needed to produce a detectable lens. In addition, for an overdensity with redshift approaching unity, there are fewer background galaxies to lens (less signal) as well as more foreground galaxies in the image (greater noise), further decreasing the observed lensing signal-to-noise ratio.

Another feature to note in Figure 4 is the difference in amplitude of $1 + \delta_{\min}^{\text{NL}}$ between the different profiles. Over most of the redshift range, the NFW profile requires the smallest overdensity in order to produce a detectable weak-lensing signal while the uniform-density sphere requires the largest. This is because the NFW profile has its mass much more centrally concentrated as compared to the uniform-density sphere. A source galaxy at some angular radius near the lens center will therefore be sheared more strongly by the former and hence produce a larger signal. A similar explanation accounts for the differences in amplitude of $1 + \delta_{\min}^{\text{NL}}$ between the non-uniform profiles.

5.2 The abundance of dark and virialized lenses

In Figure 5 we show the redshift distribution (normalized to unity) of dark and virialized lenses for the NFW, Hernquist, and isothermal-sphere profiles. Because the minimum overdensity for the uniform-density sphere was so large, the probability of detecting a lens with such a profile is negligible and hence no longer considered. For all three profiles the distribution peaks at $z \approx 0.5$ and has a full-width at half-maximum of $\Delta z \approx 0.5$. The distribution drops off at $z \approx 1$ for two reasons: the minimum overdensity is becoming increasing large since $\langle z_s \rangle \simeq 1$ and the STHC dynamics predicts fewer and fewer massive, large overdensities at these higher redshifts.

The sky density of dark lenses as a function of redshift for the same three profiles is shown in Figure 6. Depending on the density profile, we expect to find between 1 – 20 dark lenses per square degree out to $z = 1$ and virtually none at higher redshifts. The reason the Hernquist profile predicts a smaller dark-lens sky density compared with the isothermal sphere and NFW is that such a profile requires a larger overdensity to produce a detectable weak-lensing signal (see Figure 3). Finally, note that although this distribution is integrated over dark lenses of all masses, the minimum overdensity as a function of redshift becomes so large for $M \lesssim 5 \times 10^{13} M_{\odot}$ that there are virtually no dark lenses with such small masses. Furthermore,

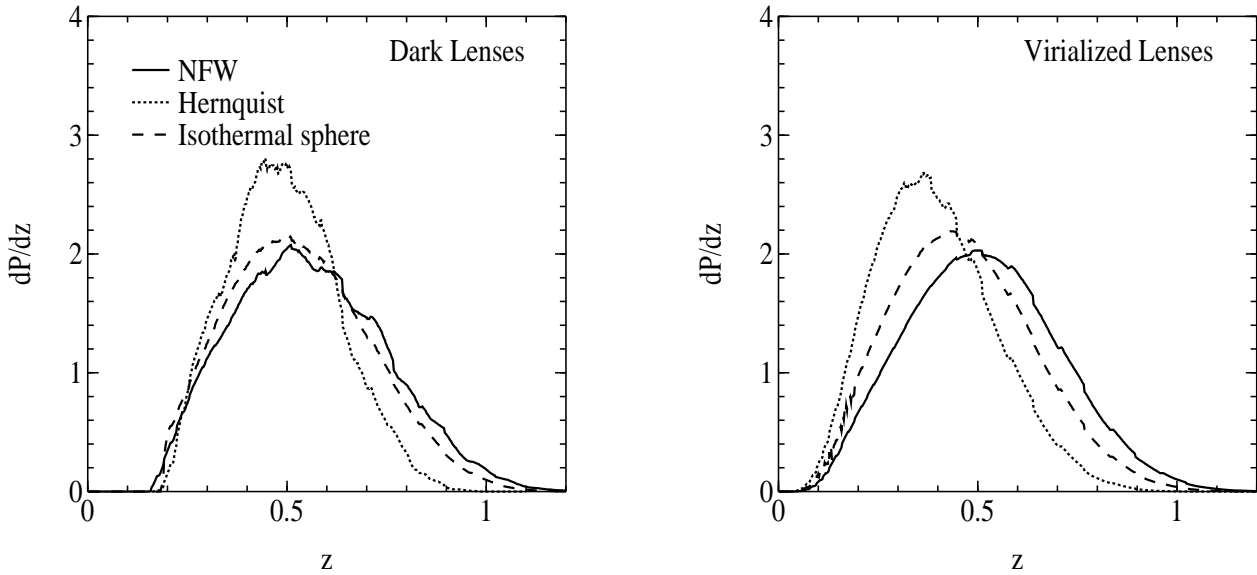


Figure 5. Redshift distribution of dark lenses (left panel) and virialized lenses (right panel) for a truncated isothermal sphere (dashed curve), an Hernquist profile (dotted curve), and an NFW profile (solid curve). The ordinate gives the normalized probability distribution per unit redshift interval.

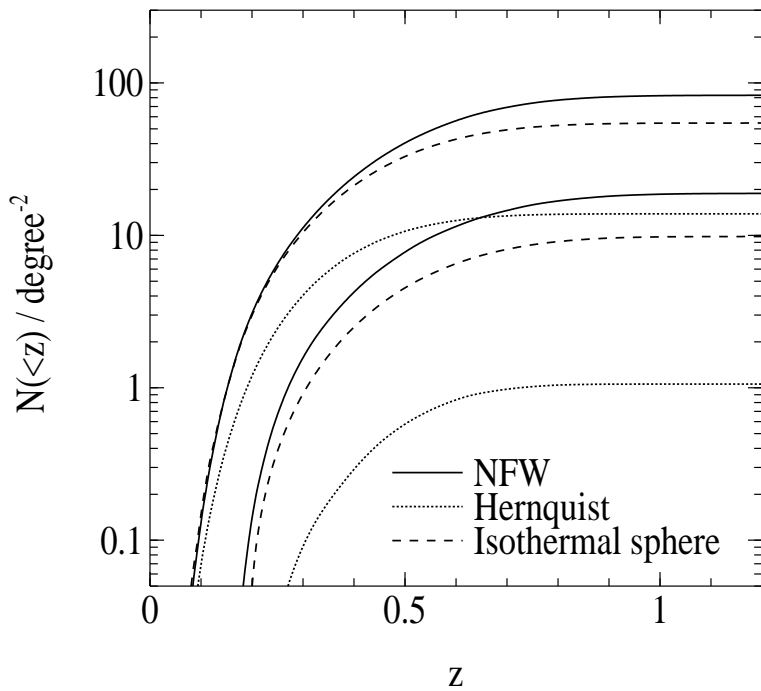


Figure 6. The number counts of dark and virialized lenses for a truncated isothermal sphere (dashed curve), an Hernquist profile (dotted curve), and an NFW profile (solid curve). The ordinate gives the sky density of lenses at redshifts less than z . The top curve for a given density profile corresponds to the sky density of virialized lenses and the bottom curve to the sky density of dark lenses.

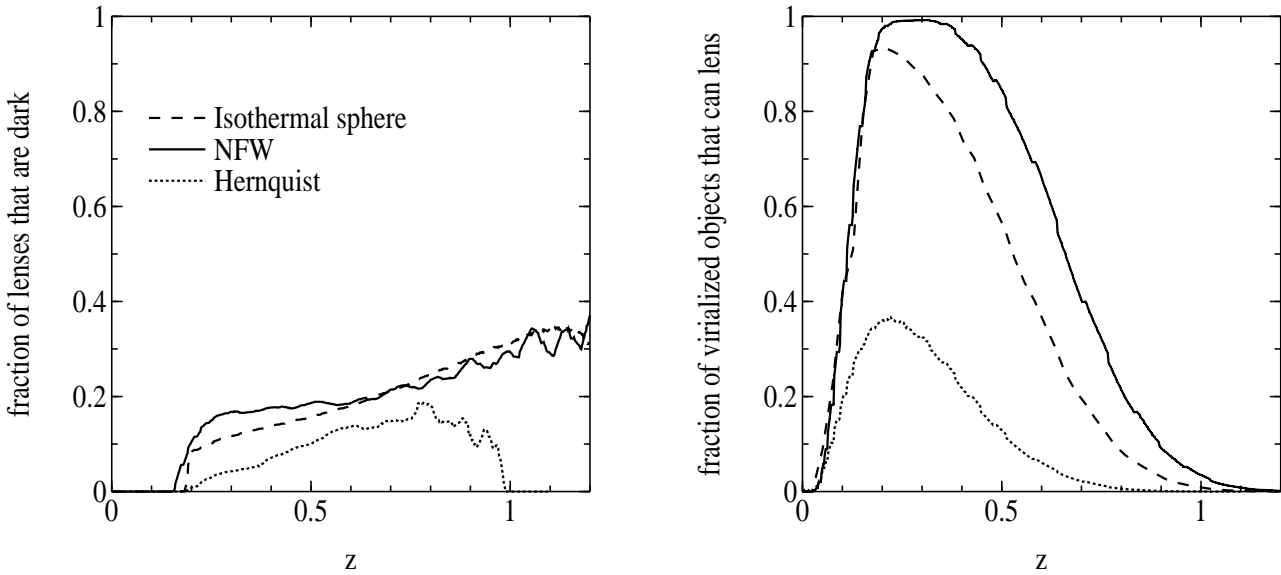


Figure 7. Left panel: The fraction of weak lenses that are dark lenses as a function of redshift for a truncated isothermal sphere (dashed curve), an Hernquist profile (dotted curve), and an NFW profile (solid curve). The fraction is relatively constant between redshifts $z = 0.2$ and $z = 1.0$, beyond which the abundance of both dark and virialized lenses drops to zero. The coarseness of the curves for $z > 1$ is an artifact of numerical noise that is a result of this drop off in both abundances. Right panel: The fraction of virialized objects with $M > 5 \times 10^{13} M_{\odot}$ that are able to weak lens as a function of redshift for the same density profiles as above.

since the Press-Schechter mass function falls off steeply with mass, there will be very few dark lenses with $M \gtrsim 10^{15} M_{\odot}$ despite the lower value of the minimum overdensity at these masses.

In Figure 5 and 6 we also show the redshift distribution and sky density of virialized lenses for the three different density profiles. Given that the virialized systems are in a mass range similar to that of the dark lenses it is not surprising that their normalized distributions are so similar. However, despite the similar distributions the sky density of virialized lenses is $10 - 80$ degree $^{-2}$ and hence a factor of $4 - 10$ larger than the sky density of dark lenses. This is because by redshifts of $z \approx 0.5$ (where the distributions peak) a majority of objects in the mass range that can lens will have already virialized.

Having computed the redshift distribution and sky density of dark and virialized lenses we now determine their relative abundances. The fraction of weak lenses that are caused by dark, non-virialized objects as a function of redshift is shown in the left panel of Figure 7. Out to $z \approx 1$ the fraction is nearly constant with about 20% of all weak lenses arising from dark objects. For $z > 1$ the abundance of weak lenses of all types (both virialized and dark) drops off significantly. This, again, is because $\langle z_s \rangle \sim 1$ and because the evolution of overdensities has not yet had enough time to produce sufficiently large overdensities. This is also illustrated in the right panel of Figure 7 where we show the fraction of virialized objects that can lens as a function of redshift. For $0.2 \lesssim z \lesssim 0.5$ a large fraction of virialized objects with $M > 5 \times 10^{13} M_{\odot}$ can produce a detectable weak-lensing signal but, for the same reason as above, by $z = 1$ this fraction is nearly zero.

5.3 The effect of increasing the image size on the lensing signal

In the above calculations we assume that the lensing images are 5 arcmin in radius, roughly the size of lensing maps to date. However, if a lens is relatively nearby or has a large radial extent it is possible that a large fraction of the total lensing signal is missed. This effect might be especially troublesome for the detection of dark lenses, given that they are not yet virialized and hence have larger radii. We now address this issue by determining the extent to which increasing the image size alters the predicted abundance of dark lenses.

In Figure 8 we plot the cumulative signal-to-noise ratio and the fraction of the total signal as a function of the angular distance from the lens center for a lens with an NFW profile at redshift $z = 0.3$ with mass $M = 10^{14} M_{\odot}$. Although the fraction of the signal that comes from within 5 arcmin is $\sim 90\%$ for lenses of overdensity $1 + \delta_{\min}^{\text{NL}} = 200$ and $1 + \delta_{\min}^{\text{NL}} = 70$ the lens with overdensity 200 requires an image size of just ~ 2 arcmin to be detectable ($S/N = 5$) while the lens with overdensity 70 requires ~ 10 arcmin to be detectable. In general we find that in order to detect nearly all dark lenses with $S/N \geq 5$ in a given field the image area must be at least $\sim \pi(15')^2 \approx 0.2$ degree 2 , as shown in Figure 9. Larger image sizes will not significantly increase the number of dark lenses detected as very little signal comes from radii larger than 15 arcmin. Also note that although lensing geometry favors a lens midway between observer and source, this effect is somewhat countered by

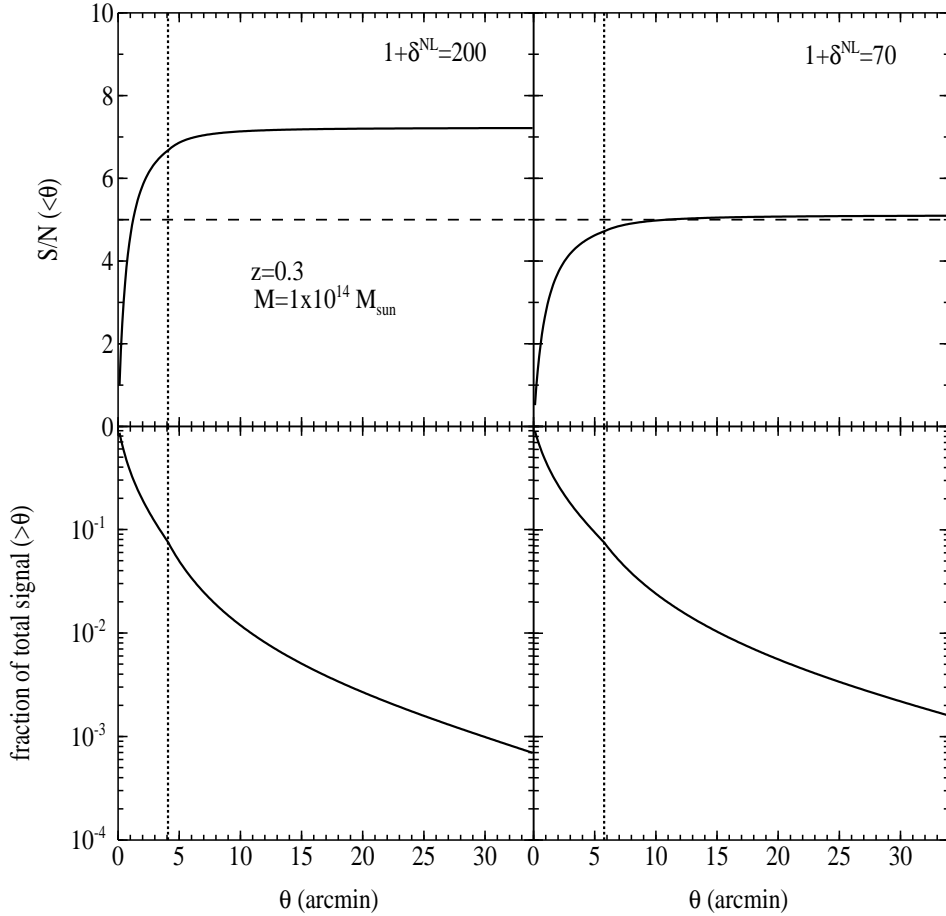


Figure 8. Upper panels: The signal-to-noise ratio within an angular radius θ from the lens center as a function of θ for an NFW profile. Lower panels: The fraction of the total lensing signal that comes from outside the angular radius θ . Approximately 90% of the lensing signal comes from a region smaller than the lensing halo radius. All four panels correspond to an object at redshift $z = 0.3$ and mass $M = 10^{14} M_{\odot}$. The left-hand-side plots are for a nonlinear overdensity of 200 and the right-hand-side plots for a nonlinear overdensity of 70.

the fact that the closer a weak lens is to the observer, the closer the source galaxy images pass to the highly overdense lens center (i.e., the solid angle subtended by the lens is larger). As a result, if the image size is large enough to enclose a large portion of the lens core, the lensing signal will be most strong when the lens-observer distance is slightly smaller than the lens-source distance. This accounts for the shift, shown in Figure 9, of the minimum of $1 + \delta_{\min}^{\text{NL}}(z)$ toward smaller redshift as the image size is increased.

5.4 Estimating σ_8 from the abundance of weak lenses

The present-day abundance of rich, X-ray clusters has been used to constrain the value of σ_8 , the amplitude of mass fluctuations in spheres of radius $8h^{-1}$ Mpc (Evrard 1989; Henry & Arnaud 1991; White, Efstathiou & Frenk 1993; Viana & Liddle 1996; Eke, Cole & Frenk 1996; Kitayama & Suto 1997, Viana & Liddle 1999). In Figure 10 we show the extent to which the measured abundance of weak lenses (from future cosmic-shear surveys, say) can further constrain σ_8 . Here we have plotted the sky density of weak lenses (both virialized and dark) at the 95% confidence limits of σ_8 given by Viana & Liddle (1999). Since weak lenses are produced by only relatively rare objects, their abundance is very sensitive to the value of σ_8 , suggesting the usefulness of weak lenses in measuring the amplitude of mass fluctuations.

Another benefit of using weak lenses to measure σ_8 is their broad redshift distribution. In particular, a systematic uncertainty in measuring σ_8 by measuring rich cluster abundances is the degeneracy between σ_8 and Ω_m that arises from the limited range in redshift in which rich clusters are observed. To break this degeneracy substantial effort is made to measure not only the present-day rich cluster abundance but also the rich cluster abundance at higher redshifts ($z \approx 0.3$; e.g., Henry

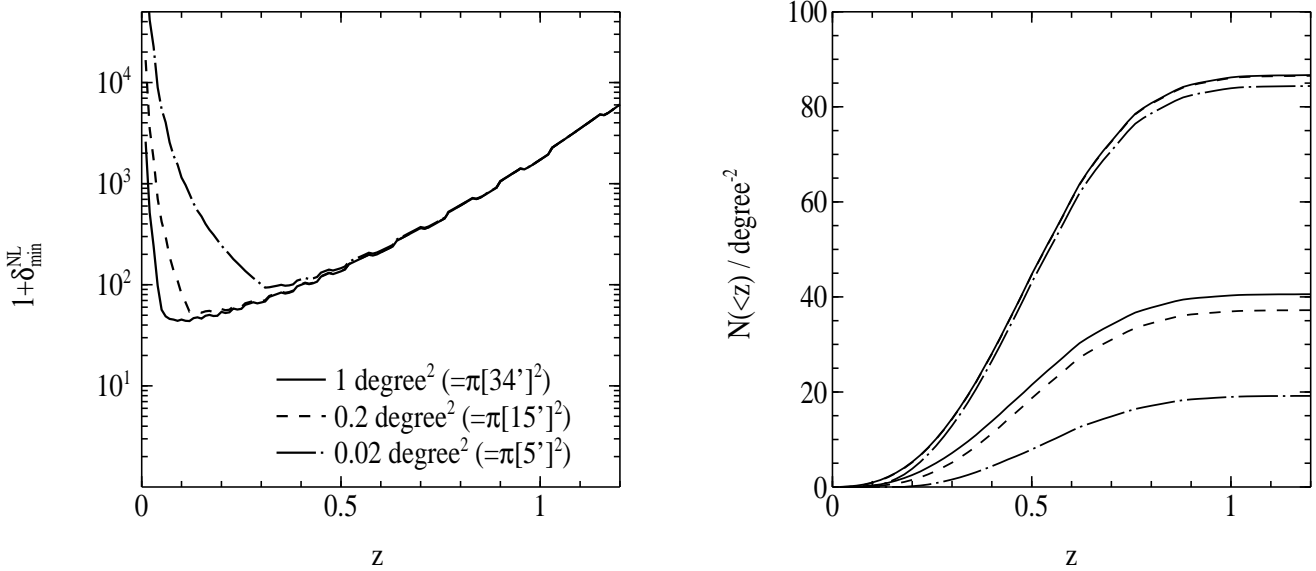


Figure 9. The effect of increasing the image size on the abundance estimates. Plotted are the minimum overdensity needed to produce a detectable lens (*left panel*) and the sky density of weak lenses (*right panel*) as functions of redshift for image sizes of 0.02 degree^2 (line-dot curve), 0.2 degree^2 (dashed curve), and 1 degree^2 (solid curve). The top three curves in the right panel correspond to virialized lenses and the bottom three to dark lenses. An NFW profile is assumed. Note that increasing the image size beyond 1 degree^2 barely increases the predicted sky density since the signal becomes increasingly small at larger angular distances from the lens center (see Figure 8).

1997). This, in turn, gives an estimate of the evolution of the cluster mass function and hence an estimate of Ω_m . However, because they are faint, detecting high redshift ($z > 0.3$) rich clusters is difficult. Weak lenses, on the other hand, do not suffer from this limitation and in fact are expected to have a broad redshift distribution and be most abundant at $z \sim 0.5$ (see Figure 5). As a result, detecting weak lenses provides an excellent means of measuring the evolution of the mass function and hence measuring Ω_m . By thereby breaking the degeneracy between σ_8 and Ω_m , weak lensing surveys are also well-suited to constrain the power-spectrum amplitude, σ_8 .

6 DISCUSSION AND CONCLUSIONS

In this paper, we have calculated the abundance of dark and virialized lenses. This was accomplished by first expressing the lensing signal strength as a function of the dark-matter overdensity and redshift. Having determined the overdensity required to produce a detectable weak-lensing signal we used the STHC model to calculate the differential abundance of overdensities as a function of position along their evolutionary cycle. Overdensities whose lensing signal yielded $S/N \geq 5$ were divided into two classes: those with $1 + \delta^{\text{NL}} < 1 + \delta_{\text{vir}}^{\text{NL}}$ were dark lenses while those with $1 + \delta^{\text{NL}} > 1 + \delta_{\text{vir}}^{\text{NL}}$ were virialized lenses.

The distinction between dark and virialized lenses was based on the former being at an unrelaxed, and hence earlier, stage in the overdensity evolutionary cycle. This distinction is not arbitrary but rather is expected to result in observational features that definitively separate the two classes of lenses. For instance, since dark lenses will typically have overdensities of $1 + \delta^{\text{NL}} \sim 100$ while virialized lenses have $1 + \delta^{\text{NL}} \sim 300$ (see Figure 4), the projected surface density of a dark lens is smaller than that in a virialized lens by a factor of $3^{2/3} \sim 2$. The sky density of galaxies in a dark lens will therefore be about two times smaller than in a virialized lens. As it is difficult to detect a significant galaxy overdensity for even a virialized, lensing, cluster at redshifts of $z \sim 0.5$, it will be all the more difficult to do so for a dark cluster. Another distinctive observational feature expected of dark lenses is a low X-ray luminosity as compared with virialized lenses, a consequence of the X-ray luminosity function's steep dependence on total virialized mass. This effect might also account for the low X-ray luminosities observed by Postman et al. (2001) in three high-redshift clusters; namely, these objects are in fact proto-clusters that have not yet completely virialized.

While we examined the predicted distribution and sky density of weak lenses for a variety of profiles, there is good reason to regard the NFW profile as the most plausible. For virialized lenses this is clearly the case as both observations and N-body simulations show that the halo density profiles are well fit by the NFW form. Though it is difficult to be as certain in the case of dark lenses (N-body simulation fits to profiles have so far only been for virialized systems), because most of the dark lenses are well past turnaround ($1 + \delta^{\text{NL}} \gtrsim 50$) and because it is unlikely that the STHC model perfectly describes the evolution of

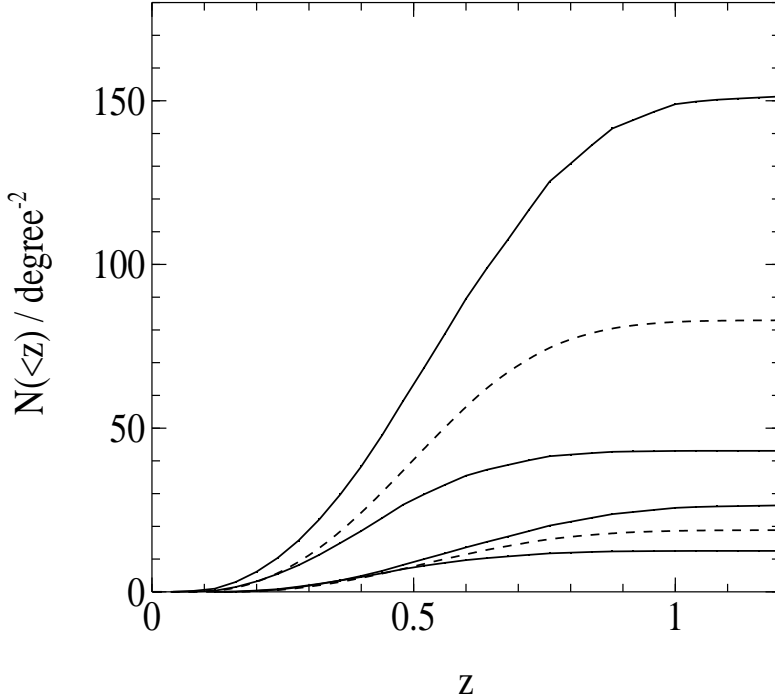


Figure 10. The predicted sky density of weak lenses at the 95% confidence limits of σ_8 (solid curves) given by Viana & Liddle (1999). The dashed curves are the predicted sky densities for the mean value of σ_8 . The top three curves correspond to virialized lenses and the bottom three to dark lenses. An NFW profile is assumed.

overdensities all the way to virialization, assuming an NFW profile for dark lenses is a fair approximation. Furthermore, since virialization is expected to occur from inside-out, the centers of dark lenses, where most of the lensing signal is coming from (see Figure 8), are likely near virialization and hence well described by the NFW profile.

That said, we have shown that the redshift distribution of dark and virialized lenses with the NFW profile is fairly broad with an average around $z = 0.5$ and a FWHM of $\Delta z \approx 0.5$. The sky density of dark lenses for the NFW profile was calculated to be $\sim 20 \text{ degree}^{-2}$ and should therefore be readily detectable by upcoming cosmic shear surveys. Given the sky coverage of weak-lensing maps to date ($\sim 1000 \text{ arcmin}^2$) and the average size of the individual lensing maps ($\sim 30 \text{ arcmin}^2$), the number of dark lenses we would expect to have seen is of order unity and thus consistent with the detection (Erben et al. 2000, Miralles et al. 2002) of one or two dark lenses. The predicted sky density of virialized lenses is $\sim 80 \text{ degree}^{-2}$, a factor of 4 to 5 larger than that of dark lenses. This difference is due to the fact that most of the weak lenses are at redshift $z \approx 0.5$ and have masses of $\sim 10^{14} M_\odot$ so that the majority are, according to the STHC model, virialized.

Finally, we have also shown that measuring the abundance of weak lenses can substantially help to constrain σ_8 , the rms mass fluctuation in spheres of radius $8h^{-1} \text{ Mpc}$. This is a consequence of the broad redshift distribution of weak lenses and the fact that they correspond to high-density peaks in the Gaussian primordial distribution. Cosmic-shear surveys, with their ability to detect cluster mass weak lenses over large areas of sky, should therefore provide a powerful new technique for determining the power-spectrum amplitude σ_8 .

ACKNOWLEDGMENTS

We thank R. Ellis for useful comments. NNW acknowledges the support of an NSF Graduate Fellowship. This work was supported in part by NSF AST-0096023, NASA NAG5-8506, and DoE DE-FG03-92-ER40701.

REFERENCES

Bacon D. J., Refregier A. R., Ellis R. S., 2000, MNRAS, 318, 625
 Bartelmann M., 1996, A&A, 313, 697

Bartelmann M., 1995, A&A, 303, 643
 Bartelmann M., Schneider P., 1992, A&A, 259, 413
 Bartelmann M., Schneider P., 2001, Phys. Rep., 340, 291
 Blandford R. D., Saust A. B., Brainerd T. G., Villumsen J. V., 1991, MNRAS, 251, 600
 Brainerd T. G., Blandford R. D., Smail I., 1996, ApJ, 466, 623
 Bullock J. S., Kolatt T. S., Sigad Y., Somerville R. S., Kravtsov A. V., Klypin A. A., Primack J. R., Dekel A., 2001, MNRAS, 321, 559
 Dalcanton J. J., Spergel D. N., Summers F. J., 1997, ApJ, 482, 659
 Eke V. R., Cole S., Frenk C. S., 1996, MNRAS, 282, 263
 Erben T., van Waerbeke L., Mellier Y., Schneider P., Cuillandre J.-C., Castander F. J., Dantel-Fort M., 2000, A&A, 355, 23
 Evrard A. E., 1989, ApJ, 341, L71
 Gray M. E., Ellis R. S., Lewis J. R., McMahon R. G., Firth A. E., 2001, MNRAS, 325, 111
 Henry J. P., 1997, ApJ, 489, L1
 Henry J. P., Arnaud K. A., 1991, ApJ, 372, 410
 Hernquist L., 1990, ApJ, 356, 359
 Kaiser N., 1992, ApJ, 388, 272
 Kaiser N., Wilson, G. Luppino G. A., 2000, astro-ph/0003338
 Kamionkowski M., Babul A., Cress C. M., Refregier A., 1998, MNRAS, 301, 1064
 Kitayama T., Suto Y., 1997, ApJ, 490, 557
 Kitayama T., Suto Y., 1996, ApJ, 469, 480
 Koopmans L. V. E. et al. (the CLASS collaboration), 2000, A&A, 361, 815
 Kruse G., Schneider P., 1999, MNRAS, 302, 821
 Lahav O., Lilje P. B., Primack J. R., Rees M. J., 1991, MNRAS, 251, 128
 Mellier Y., 1999, ARAA, 37, 127
 Miralda-Escudé J., 1991, ApJ, 380, 1
 Miralles J. M., Erben T., Haemmerle H., Schneider P., Fosbury R. A. E., Freudling W., Pirzkal N., Jain B., White S. D. M., 2002, astro-ph/0202122
 Navarro J. F., Frenk C. S., White S. D. M., 1997, ApJ, 490, 493
 Navarro J. F., Frenk C. S., White S. D. M., 1996, ApJ, 462, 563
 Navarro J. F., Frenk C. S., White S. D. M., 1995, MNRAS, 275, 56
 Peebles P. J. E., 1984, ApJ, 284, 439
 Peebles P. J. E., 1980, The Large Scale Structure of the Universe, Princeton Univ. Press, Princeton, N.J.
 Postman M., Lubin L. M., Oke J. B., 2001, AJ, 122, 1125
 Press W. H., Schechter P., 1974, ApJ, 187, 425
 Reblinsky K., Kruse G., Jain B., Schneider P., 1999, A&A, 351, 815
 Schneider P., 1996, MNRAS, 283, 837
 Seitz C., Schneider P., 1997, A&A, 318, 687
 Stebbins A., 1997, astro-ph/9609149
 Van Waerbeke L., Mellier Y., Erben T., et al., 2000, A&A, 358, 30
 Viana P. T. P., Liddle A. R., 1999, MNRAS, 303, 535
 Viana P. T. P., Liddle A. R., 1996, MNRAS, 281, 323
 Weinberg N. N., Kamionkowski M., 2002, MNRAS, in preparation
 White S. D. M., Efstathiou G., Frenk C. S., 1993, MNRAS, 262, 1023
 Wittman D. M., Tyson J. A., Kirkman D., Dell'Antonio I., Bernstein G., 2000, Nature, 405, 143
 Wittman D., Tyson J. A., Margoniner V. E., Cohen J. G., Dell'Antonio I. P., 2001, ApJL, 557, L89
 Wright C. O., Brainerd T. G., 2000, ApJ, 534, 34

APPENDIX A: DERIVATION OF THE SIGNAL-TO-NOISE RELATION FOR VARIOUS DENSITY PROFILES

Starting from equation (14), we derive the signal-to-noise relation for a point mass, a uniform-density sphere, a truncated isothermal sphere, an NFW profile and a Hernquist profile. Since these profiles are all axially-symmetric, $\langle \kappa \rangle(\theta) = \kappa(\theta)$.

(i) *Point Mass:* The dimensionless mean surface mass density within a circle of radius θ for a deflecting lens of point mass M at angular diameter distance D_d is

$$\bar{\kappa} = \frac{1}{\Sigma_{\text{crit},\infty}} \frac{M}{\pi P^2}, \quad (\text{A1})$$

where $P = \theta D_d$. The quantity κ , the dimensionless mean surface mass density on a circle of radius θ , is $\propto \delta(\theta)$, the Dirac delta function. Therefore, by equation (14), the signal-to-noise relation for a point mass is given by

$$\frac{S}{N} = \frac{\sqrt{2}\langle Z \rangle M}{\sigma_e \Sigma_{\text{crit},\infty} \pi D_d^2} \frac{\sqrt{\pi n}}{\theta_{\text{out}}} \sqrt{\left(\frac{\theta_{\text{out}}}{\theta_{\text{in}}}\right)^2 - 1}. \quad (\text{A2})$$

This can be expressed as a minimum mass needed to produce a detectable weak-lensing signal, which in useful units is

$$M_{\text{min}} = 3.7 \times 10^{13} \left(\frac{S/N}{5} \right) \left(\frac{D_d}{0.3 D_H} \right)^2 \left(\frac{\sigma_e}{0.2} \right) \left(\frac{\theta_{\text{out}}}{5 \text{ arcmin}} \right) \left(\frac{n}{30 \text{ arcmin}^{-2}} \right)^{-1/2}$$

$$\times \left(\frac{(\theta_{\text{out}}/\theta_{\text{in}})^2 - 1}{100} \right)^{-1/2} \Sigma_{\text{crit}_{\infty}} \langle Z \rangle^{-1} M_{\odot},$$

where $D_H = c/H_0$ is the Hubble distance.

(ii) *Uniform Density Sphere*: Repeating the same procedure as above but for a sphere of uniform density $\rho(r) = \rho_c$ and mass M yields the following for the surface mass density (where we use the Abel integral equation to relate volume mass density to surface mass density);

$$\kappa = \frac{1}{\Sigma_{\text{crit}_{\infty}}} \int_{-\infty}^{\infty} dz \rho(r) = \frac{2\rho_c}{\Sigma_{\text{crit}_{\infty}}} \sqrt{R^2 - P^2}, \quad (\text{A3})$$

$$\begin{aligned} \bar{\kappa} &= \frac{1}{\pi P^2} \int_0^P \kappa(P') 2\pi P' dP' \\ &= \frac{4\rho_c}{3\Sigma_{\text{crit}_{\infty}}} \left(\frac{R^3 - (R^2 - P^2)^{3/2}}{P^2} \right), \end{aligned} \quad (\text{A4})$$

where dz is along the line of sight and $R = (3M/4\pi\rho_c)^{1/3}$ is the radius of the sphere. The signal-to-noise ratio is then computed by solving equation (14) with the above relations for κ and $\bar{\kappa}$.

(iii) *Truncated Isothermal Sphere*: The radial density profile of an isothermal sphere is

$$\rho(r) = \frac{\sigma_v^2}{2\pi G r^2}, \quad (\text{A5})$$

where σ_v is the line-of-sight velocity dispersion of the particles (i.e., galaxies) in the system. The surface mass density is then given by

$$\kappa = \frac{1}{2} \bar{\kappa} = \frac{\theta_E}{2\theta}, \quad (\text{A6})$$

where $\theta_E = \sigma_v^2/G D_d \Sigma_{\text{crit}_{\infty}}$. For a truncated isothermal sphere of mass M and radius R , $M = \int_0^R dr \rho(r) 4\pi r^2 = 2\sigma_v^2 R/G$, so that

$$\theta_E = \frac{M}{2R} \frac{1}{D_d \Sigma_{\text{crit}_{\infty}}}. \quad (\text{A7})$$

Equation (14) then gives

$$\frac{S}{N} = \frac{\langle Z \rangle M}{\sigma_e \Sigma_{\text{crit}_{\infty}} D_d} \frac{\sqrt{\pi n}}{2R} \sqrt{\ln(\theta_{\text{out}}/\theta_{\text{in}})}. \quad (\text{A8})$$

(iv) *NFW Profile*: The NFW density profile is given by

$$\rho(r) = \frac{\rho_s}{(r/r_s)(1+r/r_s)^2}, \quad (\text{A9})$$

where r_s and ρ_s are the scale radius and density, respectively. The mass within radius r is then

$$M(r) = 4\pi \rho_s r_s^3 \left(\ln(1+r/r_s) - \frac{r/r_s}{1+r/r_s} \right). \quad (\text{A10})$$

Bartelmann (1996) (see also Wright & Brainerd 2000) showed that the radial dependence of the tangential shear for an NFW profile is

$$\gamma_{\text{nfw}}(x) = \bar{\kappa}(x) - \kappa(x) = \frac{\rho_s r_s}{\Sigma_{\text{crit}_{\infty}}} g(x), \quad (\text{A11})$$

where $x = \theta D_d / r_s$ and

$$g(x) = \begin{cases} \frac{8 \operatorname{arctanh} \sqrt{\frac{1-x}{1+x}}}{x^2 \sqrt{1-x^2}} + \frac{4}{x^2} \ln \left(\frac{x}{2} \right) - \frac{2}{(x^2-1)} + \frac{4 \operatorname{arctanh} \sqrt{\frac{1-x}{1+x}}}{(x^2-1)(1-x^2)^{1/2}}, & (x < 1) \\ \frac{8 \operatorname{arctan} \sqrt{\frac{x-1}{1+x}}}{x^2 \sqrt{x^2-1}} + \frac{4}{x^2} \ln \left(\frac{x}{2} \right) - \frac{2}{(x^2-1)} + \frac{4 \operatorname{arctan} \sqrt{\frac{x-1}{1+x}}}{(x^2-1)^{3/2}}, & (x > 1). \end{cases} \quad (\text{A12})$$

The signal-to-noise ratio is then

$$\frac{S}{N} = \frac{2\sqrt{\pi n} \langle Z \rangle}{\sigma_e \Sigma_{\text{crit}_{\infty}} D_d} \rho_s r_s^2 \sqrt{\int_{x_{\text{in}}}^{x_{\text{out}}} dx x g(x)^2}. \quad (\text{A13})$$

There are thus three unknowns if given an overdensity of mass M : r_s , ρ_s and R . We therefore need a third relation in addition to Equations (A10) and (A13) in order to break the degeneracy. It is obtained via the following conservation of energy argument, first put forth by Dalcanton et al. (1997) for the case of disk formation.

Assume the mass profile before collapse is a uniform sphere of radius R_i and assume that at this initial stage the system's energy is entirely gravitational ($E = -3GM^2/5R_i$). As noted by Dalcanton et al. (1997), this assumption is well motivated in the context of disk formation by the observed similarity between disk angular momentum distributions and the angular momentum distribution of a uniformly rotating sphere. It is natural to assume a similar initial condition occurs for systems at larger scales, i.e., cluster masses. As the overdensity collapses and approaches virialization, the mass distribution evolves into an NFW profile, as suggested by numerical simulations. At this stage the system's potential energy within a radius r is

$$\Phi(y) = -8\pi^2 G \rho_s^2 r_s^5 \left(1 - \frac{2y \ln y + 1}{y^2} \right), \quad (\text{A14})$$

where $y \equiv 1 + r/r_s$. Assuming the energy of the overdensity within R_i is conserved during collapse and that the system is near virialization so that $E \approx |\Phi|/2$ then gives $R_i = 8.74r_s$. Since the truncation radius is given by the radius that contains mass M , by conservation of mass $R = R_i = 8.74r_s$ (i.e., though the mass is redistributed as the overdensity evolves the size of the sphere containing mass M is constant in time). When we include the effects of the cosmological constant in the conservation of energy argument there is little change in the result. The above relation between R and r_s thus provides the sought after third equation needed to break the degeneracy between r_s , ρ_s and R . In an upcoming paper (Weinberg & Kamionkowski 2002) we show that the above approach yields concentration parameters that are slightly different from those obtained by N-body simulations (i.e., Bullock et al. 2001). Nonetheless, the concentration parameters obtained by the two approaches predict a similar abundance of virialized lenses. Note that since the N-body simulations fit the concentration parameters to virialized objects, the above analytic approach must be used in order to compute the abundances of dark lenses.

(v) *Hernquist Profile*: The Hernquist profile is given by

$$\rho(r) = \frac{M_\infty}{2\pi} \frac{1}{(r/r_s)(r+r_s)^3}, \quad (\text{A15})$$

where r_s is the scale radius and M_∞ is the mass enclosed at infinity. The mass within radius r is then

$$M(r) = M_\infty \left(\frac{r/r_s}{1 + r/r_s} \right)^2. \quad (\text{A16})$$

Using the Abel integral equation it can be shown that the dimensionless surface mass density for the Hernquist profile is

$$\kappa(x) = \frac{M_\infty}{\pi r_s^2 \Sigma_{\text{crit},\infty}} f(x), \quad (\text{A17})$$

where $x = \theta D_d/r_s$ and

$$f(x) = \begin{cases} \frac{1}{(x^2-1)^2} \left[\frac{(2+x^2)\text{arctanh}\sqrt{\frac{1-x}{1+x}}}{\sqrt{1-x^2}} - \frac{3}{2} \right], & (x < 1) \\ \frac{1}{(x^2-1)^2} \left[\frac{(2+x^2)\text{arctan}\sqrt{\frac{x-1}{1+x}}}{\sqrt{x^2-1}} - \frac{3}{2} \right], & (x > 1) \end{cases} \quad (\text{A18})$$

The dimensionless surface mass density within x is then,

$$\bar{\kappa}(x) = \frac{2}{x^2} \frac{M_\infty}{\pi r_s^2 \Sigma_{\text{crit},\infty}} \int_0^x dx' x' f(x'). \quad (\text{A19})$$

The signal-to-noise ratio is then obtained by inserting the above relations into equation (14).

As in the case of the NFW profile, given an overdensity of mass M , there are three unknowns. We therefore apply the same energy conservation argument as above, assuming the overdensity is initially a uniform density sphere of radius R_i and upon collapse relaxes to a Hernquist profile. The potential energy upon collapse is

$$\Phi(y) = -\frac{GM_\infty^2}{6r_s} \left(1 - \frac{6y^2 - 8y + 3}{y^4} \right), \quad (\text{A20})$$

where $y = 1 + r/r_s$. Assuming energy conservation and a nearly virialized overdensity yields $R = R_i = 3.2r_s$, allowing us to solve the signal-to-noise relation.